

VU Research Portal

Structural and spectroscopic in vivo imaging of the human retina with scanning light ophthalmoscopy

Damodaran, M.

2020

document version

Publisher's PDF, also known as Version of record

[Link to publication in VU Research Portal](#)

citation for published version (APA)

Damodaran, M. (2020). *Structural and spectroscopic in vivo imaging of the human retina with scanning light ophthalmoscopy*. [PhD-Thesis - Research and graduation internal, Vrije Universiteit Amsterdam].

General rights

Copyright and moral rights for the publications made accessible in the public portal are retained by the authors and/or other copyright owners and it is a condition of accessing publications that users recognise and abide by the legal requirements associated with these rights.

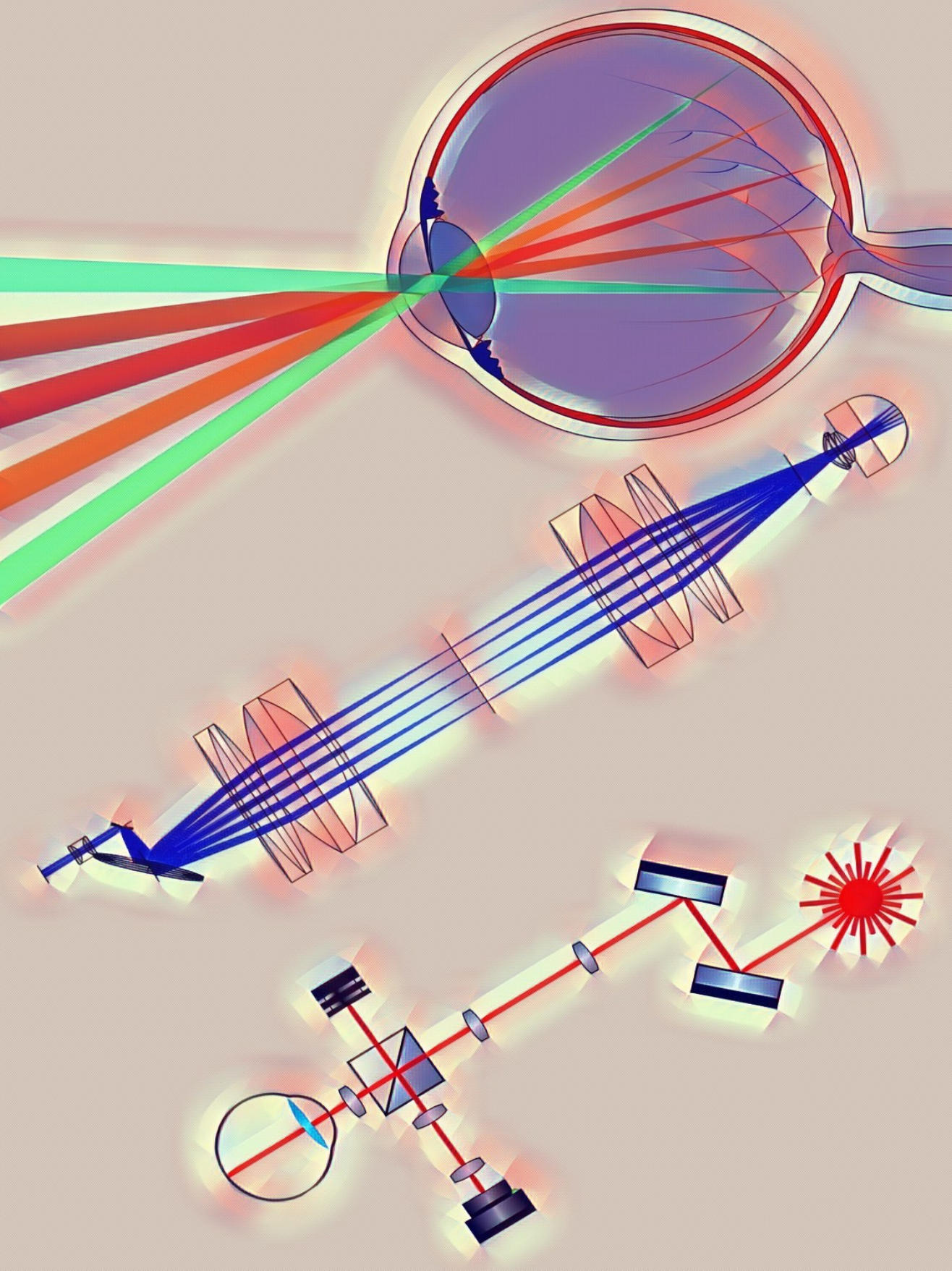
- Users may download and print one copy of any publication from the public portal for the purpose of private study or research.
- You may not further distribute the material or use it for any profit-making activity or commercial gain
- You may freely distribute the URL identifying the publication in the public portal

Take down policy

If you believe that this document breaches copyright please contact us providing details, and we will remove access to the work immediately and investigate your claim.

E-mail address:

vuresearchportal.ub@vu.nl



2

Principles of retinal imaging and retinal oximetry

Overview

Modern retinal imaging systems produce dynamic, high-resolution images at low irradiation at a high frame rate. Continuous acquisition of high-contrast images of the retina and other structures in the ocular fundus is possible. An excellent example of a system which benefits from this versatility is a Scanning Laser Ophthalmoscope (SLO). The SLO is a tool that has expanded the therapeutic and diagnostic abilities of retinal imaging not only through qualitative imaging but also through added techniques such as perimetry and angiography. The SLO is comparable in its scope of application and utility to Optical Coherence Tomography (OCT), and both these imaging techniques complement each other perfectly. In this chapter, we outline the principles of scanning-based retinal imaging by using a digital micromirror device (DMD) or a pair of scanning mirrors to produce high contrast images of the human retina. As an important application of retinal imaging, measuring oxygen saturation from the retina is introduced in this chapter in detail as well.

2.1 Retinal imaging by scanning

The first effort to introduce an ophthalmic imaging technique which would not suffer from the limitations of fundus photography was the SLO [1–6]. In the SLO, a narrow beam of 2–4 mm diameter is focused by the cornea and lens to a single point of $\sim 10\text{ }\mu\text{m}$ in the retina. An image is produced by scanning the beam over the retina usually in a raster pattern and detecting the reflected light from each scan point, to produce a digital image. Beam deflection is typically achieved by a combination of two galvanometer scanners, one slow scanner and one fast scanner, to provide scanning in both horizontal and vertical directions. A basic design of an SLO is given in Fig. 2.1.

Widefield imaging systems such as the fundus camera (see section 1.2.1) suffer from corneal back reflections. To avoid these strong reflections, typical fundus camera employs annular illumination where the annulus is imaged on to the pupil. The reflected light from the retina is collected only through a small central spot of the pupil. In contrast, the SLO illuminates a narrow beam through a central portion of the pupil and the reflected light is collected over the entire pupil. This results in increased light collection efficiency, and with a confocal arrangement consisting of illumination and detection pinholes to reject out-of-focus light, the confocal SLO (cSLO) rejects corneal reflections and further increases resolution and contrast through confocality. A pair of scanners are used to construct a two-dimensional scan [7]. The generalised design is described in Fig. 2.1. A Common optical path-

way (relay telescope) for illuminating and collecting reflected light from the retina is split into separate paths near the source and the detector. The relay telescope can be made of either lens or curved, and the beam diameter and the focal length of these focusing elements (A and B in Fig. 2.1) determine the magnification and the size of the beam on the pupil plane. For a magnification (M), the size of the beam in the pupil plane is given by $M \times \omega_0$, where ω_0 is the size of the collimated beam from the source. The diffraction-limited spot size (d_{spot}) on the retina considering an aberration-free eye lens of focal length f_{eye} is then,

$$d_{spot} = \frac{2 \cdot \lambda_{ill} \cdot f_{eye}}{\pi \cdot (M \times \omega_0)} \quad (2.1)$$

where λ_{ill} is the illumination wavelength. The combined optical power of both the cornea and the crystalline lens focuses the light onto the retina. The power of this simplified eye model is 60 D and has a corresponding focal length f_{eye} of 16.7 mm in air. The critical design parameters of the SLO design are the Field-of-view (FOV) and frame rate (frames/s).

In retinal imaging, the diameter of the pupil, d_{pupil} is usually the limiting aperture limiting the amount of light entering the eye. Under normal conditions, d_{pupil} remains at around 2-3 mm and reaches 6-7 mm with dark adaptation or with the application of pupil dilating eye drops such as tropicamide. The number of frames per second or the imaging frame rate is given by the ratio of the fast scanning frequency to the number of lines per each recorded frame. i.e.,

$$frames/s = \frac{2 \times resonant frequency}{lines/frame} \quad (2.2)$$

One disadvantage of using a resonant scanning mirror in the SLO is that it introduces distortion into the recorded image due to the non-constant scan velocity of the scanning mirrors. With a resonant mirror, the position of the laser changes with a sinusoidal motion of the mirrors. As a result, the image obtained is stretched progressively towards the edges. The image should be corrected for this sinusoidal distortion, as illustrated in Fig. 2.2.

2.1.1 Line scanning

Line scanning SLO (LSLO) [3, 6] uses an anamorphic optical element such as a cylindrical lens to create a line illumination on the retina in one dimension. Only one scanning mirror is needed to scan the beam in the other dimension. A slit

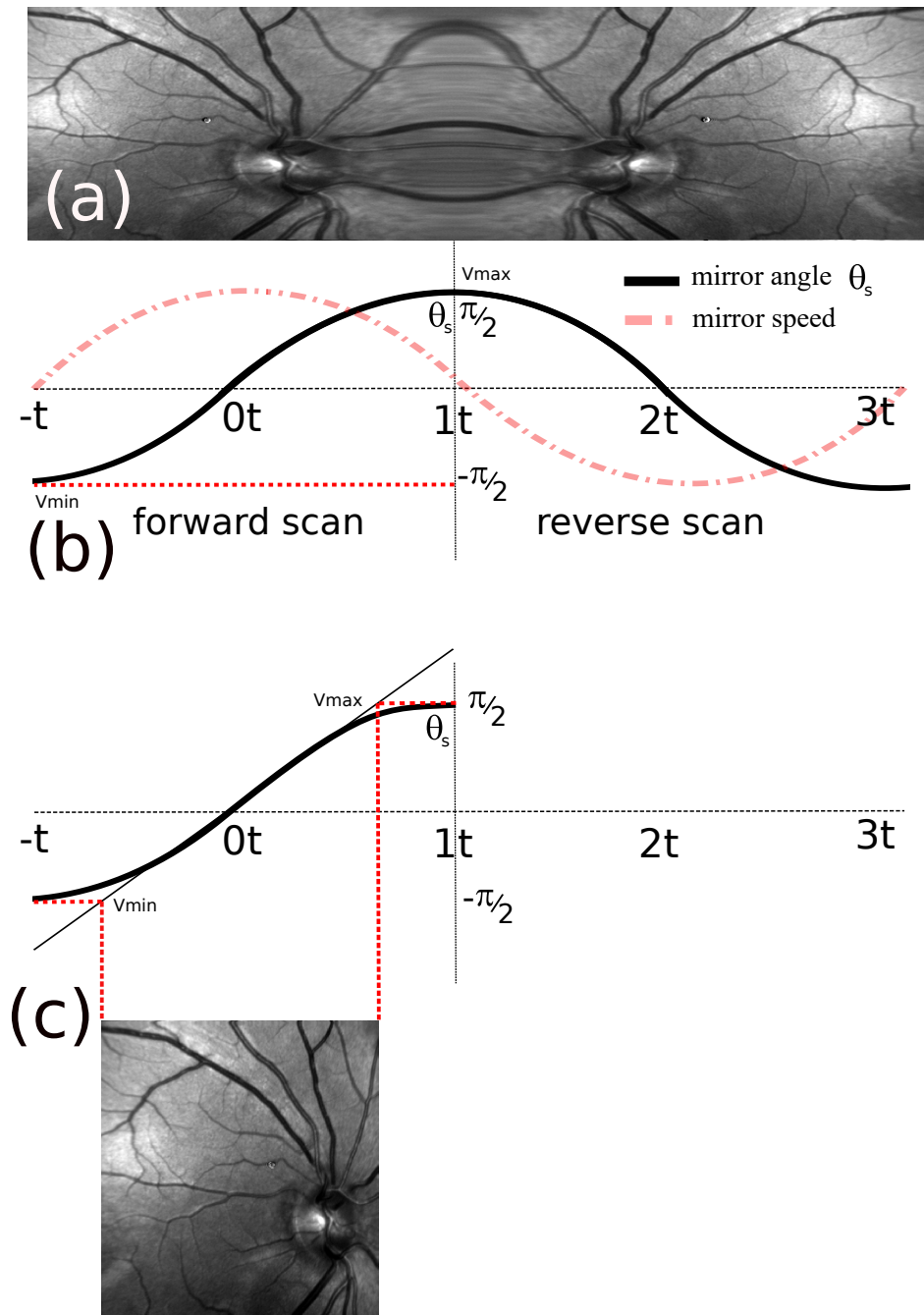


Figure 2.2: Image correction for resonant scanners — (a): Half-height, double-width images collected by a fixed frequency pixel clock. The mirrored-image is collected by the forward and reverse scan of the resonant mirror. (b): The relationship between the mirror angle θ_s and the mirror velocity during the forward and the reverse scan (c): the correction factor is determined by the ratio of the actual mirror motion and the predicted linear motion. The pixels are then reassigned as shown in the corrected image.

aperture instead is placed of the circular aperture in the conjugate plane; a line detector is used in place of a point detector. With the LSLO, the scattered light is rejected in only one dimension, and thus there is reduced confocality compared to the confocal SLO. However, the imaging speed of the LSLO is significantly higher compared to the confocal SLO. The improvement in the imaging speed scales with the square root of the same FOV since the scanning is only in one dimension for the LSLO. Further, for line projection onto the retina, the maximum permissible exposure is higher compared to conventional SLO. For a detailed description of the principle and construction of an LSLO, the readers are pointed towards Hammer *et al.* [3].

2.1.2 Digital micromirror devices

To reduce the cost and complexity of an SLO, Digital micromirror devices (DMDs) are used as an alternative to galvo scanners. DMDs are based on microscopically small mirrors that are controlled by applying a voltage or current between the two electrodes around the mirror arrays. The DMD is both a micro-electronic mechanical system (MEMS) and a spatial light modulator (SLM). It is a MEMS because it consists of hundreds of thousands of moving micromirrors that are controlled by underlying CMOS electronics, as shown in Fig. 2.3. The spatial light modulator technology pioneered by Texas instruments evolved into the invention of the DMD by Dr Larry Hornbeck in 1986 [8]. The number of mirrors corresponds to the resolution of the projected image. These mirrors can be repositioned rapidly to reflect light either into the desired direction or onto a light dump. To produce greyscales, the mirror is toggled on and off very quickly, and the ratio of on-time to off-time determines the shade produced (binary pulse-width modulation). Liquid crystal devices (LCDs) are also widely-used as SLMs in either transmission or reflection but do not have the speed, precision, or broadband capability that makes the DMD so attractive for many applications.

DMDs have been used for retinal imaging by projecting a series of scan patterns [5, 6, 9, 10] without using conventional scanning mirrors. The DMD provides temporal and spatial flexibility for illumination, which can have several advantages, such as optimising the system for speed and confocality.

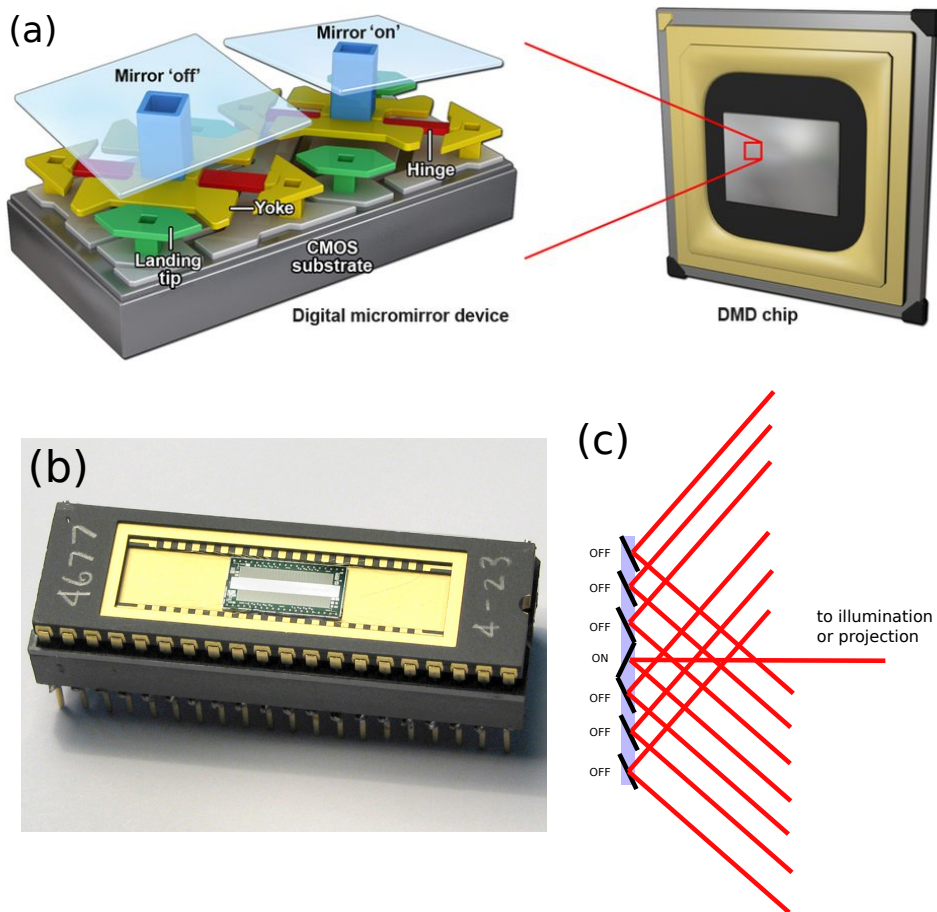


Figure 2.3: (a): DMD construction — a pair of micromirrors are zoomed in from a DMD chip showing the 'ON' and 'OFF' state of the DMD with the corresponding directions of flipping. Each micromirror is attached to a yoke and is connected to the CMOS substrate (image courtesy of [11]). (b): one of the earliest prototypes of the DMD chip. The descendants of this chips can be found in many applications today (image courtesy of *ti.com*). (c): Simplified working of the DMD showing the light from the 'ON' mirrors are directed towards an axis which can be used for projection or illumination while the light from the 'OFF' mirrors are deflected away.

2.2 Retinal imaging — optical considerations, laser safety and wavelength ranges

2.2.1 Optical considerations

Aberrations in the eye

The human eye is a simple optical device with only two elements: the cornea and the crystalline lens. However, there is no good model of the optics of an individual eye due to large interpersonal variations and changes in the optical quality and characteristics with age. The optical quality of the focusing structures in the eye affects the imaging quality. The optical aberrations in the eye affect the resolution [13], and any optical opacity in the crystalline lens or the cornea for the imaging wavelength is detrimental to the imaging quality. The defocus error in most SLOs, including the SLOs in this thesis were corrected by translating the ophthalmic lens (last lens before the cornea) to achieve sharp images. For multispectral imaging of the retina (as described in **Chapter 5 and 6**) the significant chromatic dispersion of the optics of the eye [14] had to be considered for the design of the optics. This chromatic dispersion leads to longitudinal chromatic aberration (LCA) and transverse chromatic aberration (TCA). The magnitude of LCA is about 2.5 D for visible wavelengths between 400 and 700 nm [15] while between 700 and 900 nm, the value of LCA was ~ 0.4 D [16]. LCA also shows less interpersonal variation and is considered to be independent of age [17, 18]. TCA can be corrected (partially) by post-processing techniques by warping the images of different colours to match. Powell [19] suggested the idea of correcting LCA with a lens having opposite dispersion of the eye. Zawadzki *et al.* [20] used such an achromatising lens or dispersion compensating lens (DCL) for Ultrahigh-resolution OCT. Various other groups have used these lenses for OCT and SLO applications [21–23]. In our multi-colour SLO, sharp images at multiple wavelengths were required; therefore, we implemented LCA correction. The simulation of such a DCL in the common path of the SLO is shown in Fig. 2.4.

Optical properties of the retina

The fundamental optical properties of biological tissues such as the retina can be used for the diagnosis of various diseases. A clear understanding of optical properties is thus critical for understanding the quantitative changes in the retina. The optical properties influence the propagation of light in the retinal tissues and vasculature. Thanks to the transparency of the anterior ocular media, ophthalmologists can

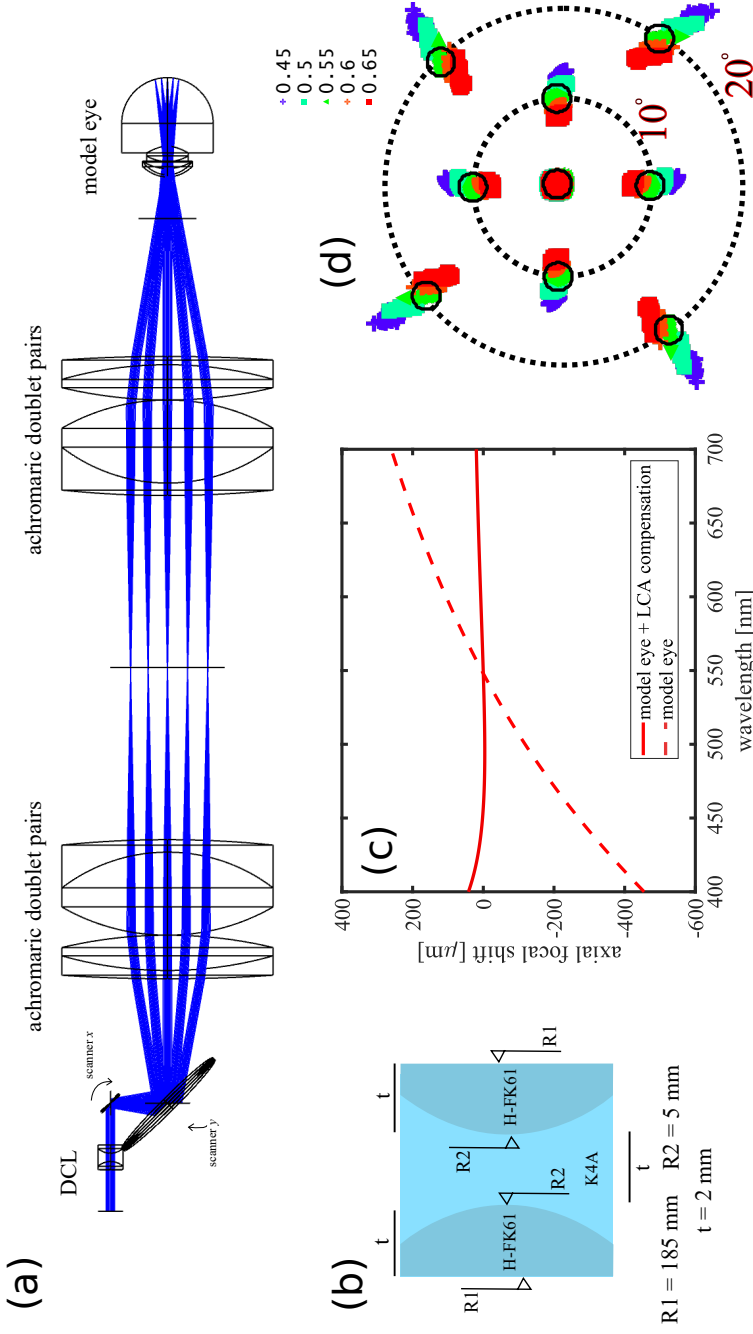


Figure 2.4: (a): Zemax simulation of SLO common path — a zero power dispersion-compensating lens (DCL) was placed in the collimated portion of the beam before the scanners. A telescope comprising of two achromatic doublet pairs was used to image the pivotal point in between the scanners on to the pupil plane. A model eye matching the physical parameters of a healthy human eye was used in the simulation [24]. (b): Design of the DCL with relevant radii and thicknesses. The materials used were H-FK61, and K4A (CDGM catalogue, Universal photonics inc., USA) (c): focal shift at the surface of the retina of the eye model from 400 to 700 nm after passing through optics shown in (a) is shown by the red dashed line. After correction with the DCL (shown by a red line), the focal shift is corrected between the colours. The maximum focal shift range is 40 μm and 0.62 mm for the system with and without correction, respectively. (d): The TCA between different wavelengths from 450 nm to 650 nm show as spot diagrams. The black circle represents the diffraction limit. TCA can be compensated partially by performing an image transform to match the different colours at the same spatial location.

have a direct look into the posterior non-transparent part of the eye. Optical analysis of the emitted light from the fundus has been used to investigate the metabolism and pathology of the retina [25]. Inhomogeneities in the retina arising from the cell components cause scattering [26], while pigments such as haemoglobin and melanin cause absorption. The corresponding wavelength-dependent optical parameters are the scattering coefficient of μ_s [mm^{-1}], the scattering anisotropy g [-], and absorption coefficient μ_a [mm^{-1}].

Melanin, a dark-brown pigment present in the RPE of the retina, is the primary component for light scattering and absorption in the fundus. Blood is confined to the retinal vasculature and scatters light. However, the most prominent optical characteristic of blood is the absorption as can be readily seen in Fig. 2.5.

Haemoglobin light absorbance

The light is absorbed and scattered in blood by the discoid-shaped erythrocytes. This optical behaviour is a result of the highly concentrated haemoglobin (Hb) content of the cell. Haemoglobin (Hb) is the most vital component in human blood and is responsible for transporting oxygen. Haemoglobin is composed of four heme groups. Each of these four heme groups contains one Fe^{2+} ion, which can bind one oxygen molecule. Haemoglobin shows distinct absorption peaks in the visible range based on the oxygenation of the Haemoglobin molecule, as shown in Fig. 2.5(b). There are many types of Hb, but Hb-A is the most abundant in healthy adult humans [27]. During inhalation of normal atmospheric air, around 9 mmol/L of oxygen is bound to haemoglobin [28]. Oxygen saturation (S) is defined as the proportion (or more often, percentage) of Hb that is bound to oxygen.

$$S = \frac{[HbO_2]}{[Hb] + [HbO_2]} \quad (2.3)$$

where $[HbO_2]$ and $[Hb]$ are the concentration of the oxy- and deoxy-Hb, respectively. Oxy- and deoxy- Hb has different colours and thus, different absorption, as shown in Fig. 2.5(a). This difference in absorption spectrum can be used to determine the oxygenation of blood by spectroscopy, an aim of this thesis. However, at certain wavelengths, the absorption is the same, and these points are called as 'isosbestic' wavelengths (Fig. 2.5(b)).

2.2.2 Laser Safety considerations in retinal imaging

Intentional exposure of light radiation on the eye for retinal imaging is a major safety concern and strict safety standards are in place to ensure safety during imag-

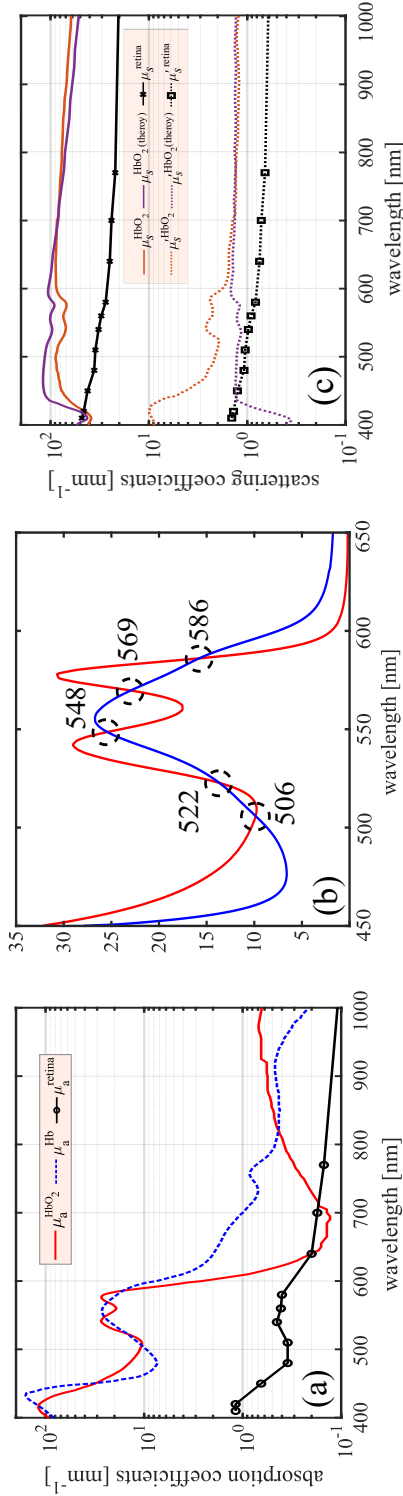


Figure 2.5: (a): Absorption spectrum of oxy- and deoxyhaemoglobin from 400 nm to 1000 nm assuming a concentration of 150 mg of haemoglobin in 1 mL of blood [29]. The absorption spectrum of neural retina measured *in vitro* by Hammer *et al.* [26] is shown for comparison. (b): The absorption spectrum from 450 nm to 650 nm on a linear scale. The absorption of these two types of haemoglobin is different for most wavelengths except for the isosbestic points (denoted by black dashed circles: 506 nm, 522 nm, 548 nm, 569 nm, and 586 nm) where the absorption depends on factors other than the 'oxygen saturation'. (c): The theoretical and experimental scattering coefficient of whole blood from Bosschaart *et al.* [30] in the 400 nm to 1000 nm regime showing a strong scattering of blood. The scattering, reduced scattering coefficient of retina [26] is shown for comparison.

ing. Damage to retina due to light exposure is caused by two mechanisms namely thermal damage and photochemical damage [31]. *Thermal damage* occurs due to temperature increase caused by melanin absorption in the RPE causing denaturation of proteins [32, 33]. The *photochemical damage* occurs in the wavelengths between 400 and 600 nm for duration longer than a second due to photo-oxidation in the photoreceptors and lipofuscin pigments [34, 35]. The biological effects of laser radiation on the eye is given in Table 2.1.

Table 2.1: Biological effects of laser radiation on the eye [31]

UV-A (315-400 nm)	Photo-chemical damage, Cataract
Visible (400-780 nm)	Photo-chemical and thermal retinal injury, Colour and night vision degradation
Infrared A (780-1400 nm)	Retinal burns, Cataract
Infrared B (1400-3000 nm)	Corneal burn, aqueous flare, IR Cataract

Calculations for the maximum permissible exposure (MPE) on the retina were performed using the latest laser safety standard IEC 60825-1 published in 2014 [36]. The most conservative estimate of the maximum permissible exposure (MPE) can be obtained by assuming a collimated, static beam entering the eye. A limiting aperture (LA) to determine MPE for the eye was taken to be 7 mm (diameter). A 7 mm LA equals an area of $3.85 \times 10^5 \text{ m}^2$ [m^2]. The accessible emission limit (AEL) was then calculated as,

$$AEL = MPE \times LA \quad (2.4)$$

From the IEC standard, the AEL expressed as irradiance or radiant exposure for a wavelength range from 450 nm to 1150 nm for a collimated beam (the correction factors for AEL calculation : $C_6 = 1$, $C_7 = 1$) with exposure time of 10 seconds or longer is given by,

$$AEL = \begin{cases} 10^{0.02 \cdot (\lambda - 450)} [W m^{-2}] \times 3.85 \times 10^{-5} [m^2] & 450 \leq \lambda \leq 500 \\ 10 [W m^{-2}] \times 3.85 \times 10^{-5} [m^2] & 500 \leq \lambda \leq 700 \\ 10 \cdot 10^{0.002 \cdot (\lambda - 700)} [W m^{-2}] \times 3.85 \times 10^{-5} [m^2] & 700 \leq \lambda \leq 1150 \end{cases}$$

The calculated AEL based on the standard is shown in Fig. 2.6. In chapter 3, we used concentric circle illumination on the retina, which extends to the whole field of view. The most conservative estimate of the AEL can be obtained by assuming a collimated static beam entering the eye. For the limiting aperture, a pupil size

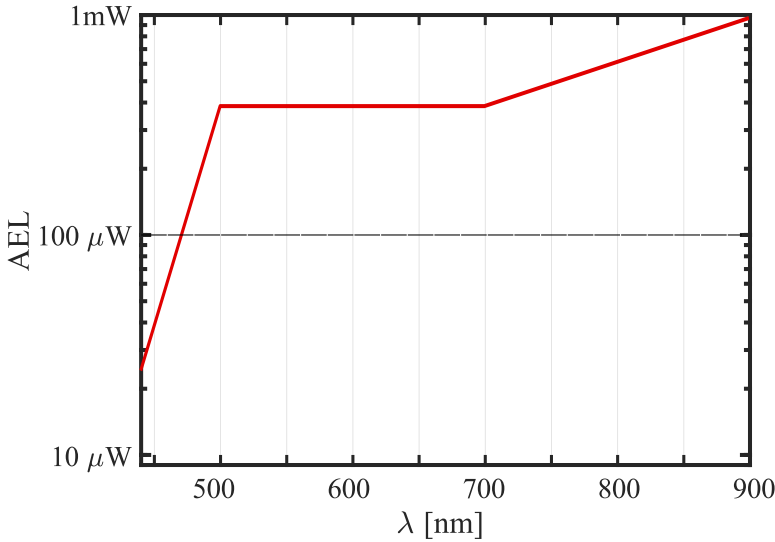


Figure 2.6: The accessible emission limit for different wavelengths for 8 hrs 20 min (30000 seconds) continuous, single point exposure— based on IEC 60825-1.

of 7 mm was used. Thus, based on Fig. 2.6, a limiting AEL of 630 μW was used. However, concentric circles are projected within the whole FOV, and the power is distributed amongst all of the circles. If the illumination of the retina is assumed to be what the standard calls extended view, the MPE limit will be more than an order of magnitude higher.

In chapters 4-6, scanners were used to scan multiple wavelengths in the whole FOV. In this case, the following criterion was used to ensure safety:

$$\frac{P(\lambda_1)}{AEL(\lambda_1)} + \frac{P(\lambda_2)}{AEL(\lambda_2)} + \frac{P(\lambda_3)}{AEL(\lambda_3)} + \dots \leq 1 \quad (2.5)$$

Where the $P(\lambda)$ is the applied power per wavelength divided by the corresponding $AEL(\lambda)$ value, based on the AEL and the detector sensitivity, the ratio of $P(\lambda)$ and $AEL(\lambda)$ was chosen suitably for optimum image quality.

Significant increase in AEL can be obtained by considering a line or area illumination in the retina instead of a spot illumination. In chapter 3, we describe a DMD based ophthalmoscope to scan multiple concentric circles on the retina. In chapters 5 and 6, we use an SLO with a resonant scanner and a galvo scanner, where the fast scan can be considered as a line projection on to the retina. Figure 2.7 shows the AEL for line projection in the retina, where it can be observed that the AEL is significantly higher compared to Fig. 2.6. However, in the *in vivo* experiments in

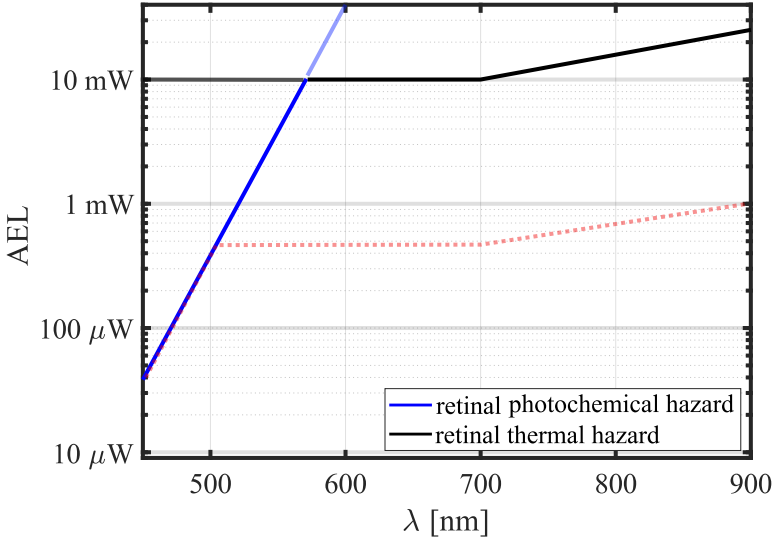


Figure 2.7: The accessible emission limit for a line projection at different wavelengths based on IEC 60825-1. The following parameters were used to arrive at this graph : $\alpha_{min} = 1.5$ mrad, $\alpha_{max} = 100$ mrad (see IEC 60825-1). The dotted red line corresponds to single point exposure for 8 hrs 20 mins (Fig. 2.6).

chapters 5 and 6, conservative AEL based on Fig. 2.6 was used.

2.2.3 Light sources and signal to noise estimation

Ophthalmic imaging, like any tissue imaging, requires a suitable wavelength of light based on the tissues which light has to traverse. Different types of tissues affect image quality and information as they absorb and scatter differently. In retinal imaging, light has to travel through a 25 mm column of vitreous humour before reaching the retina. The vitreous is 99% water, and hence highly absorbs ultra-violet (UV) and infra-red (IR) light. As a result, wavelengths roughly shorter than 400 nm and longer than 1100 nm are not usually chosen for retinal imaging. There are other essential factors to consider the wavelength choice based on the application (which is described in **Chapter 4**), and safety, as explained in section 2.2.2.

A simplified model of how a pixel grey value is created is shown in the Figure 2.8. The number of photons (mean = μ_p , variance = σ_p^2) hitting the sensor during the exposure time t_{exp} are converted to electrons (mean = μ_e , variance = σ_e^2) with a wavelength dependent quantum efficiency $\eta(\lambda)$. The number of electrons fluctuates statistically with a *Poissonian distribution* whose mean and standard deviation

are the same. Thus,

$$\mu_e = \sigma_e^2 \quad (2.6)$$

The noise arising due to particle nature of electrons and photons is called *shot noise*

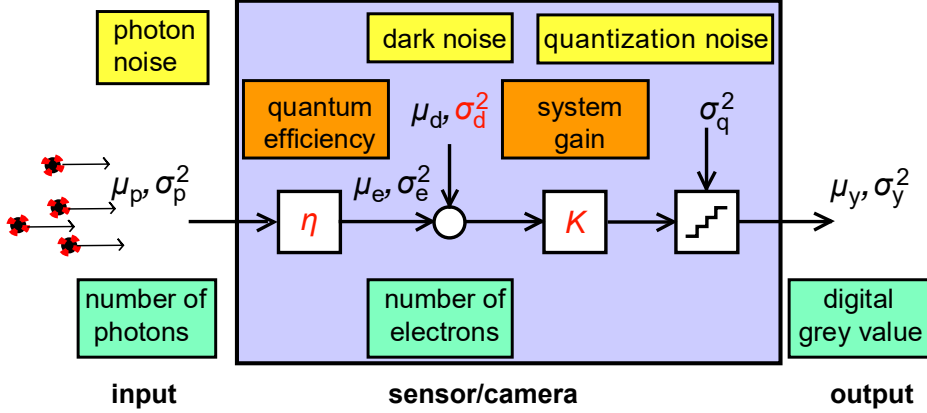


Figure 2.8: Noise model of a detector sensor or camera adapted from EMVA standard [37] showing how a grey value is generated. The mean values are represented as $\mu_{(\cdot)}$, and the variance as $\sigma_{(\cdot)}^2$, respectively. K is the system gain and η is the quantum efficiency. The intrinsic detector parameters are in red.

and the performance of all imaging systems is limited by shot noise. All noise sources related to the detector read-out and amplifier can be described by a signal independent, normal distributed noise source called *thermal noise* with variance σ_d^2 . The mean electrons are digitised to a grey value (mean = μ_y , variance = σ_y^2) with a overall gain of K and this process suffers from *quantization noise* (variance = σ_q^2). The noise adds up in an linear fashion and we can write

$$\sigma_y^2 = K^2 \cdot (\sigma_d^2 + \sigma_e^2) + \sigma_q^2 \quad (2.7)$$

This equation is central to a noise-figure estimation of any imaging system. The signal to noise ratio (SNR) can then be defined in terms of grey values as

$$SNR = \frac{\mu_y - \mu_{dark}}{\sigma_y} \quad (2.8)$$

or in terms of number of photons as

$$SNR(\mu_p) = \frac{\eta \cdot \mu_p}{\sqrt{\sigma_d^2 + \sigma_q^2/K + \eta(\lambda) \cdot \mu_p}} \quad (2.9)$$

This means that the SNR increases linearly at low irradiation when dark and quantisation noise dominate shot noise to a slower square root increase at high irradiation when shot noise dominates dark noise and quantisation noise. In this thesis, there are two types of light sources used for retinal imaging namely a LED at 810 nm (**Chapter 3**) and a supercontinuum light source for visible wavelengths (**Chapter 4-6**).

2.3 Retinal Oximetry

As was mentioned in **Chapter 1**, one of the main focuses of this thesis is measuring blood components such as oxygenation in retinal blood vessels. Blood flow within the retinal vasculature supplies oxygen and nutrients to the retinal layers and helps to dispose of waste products [38]. Maintenance of normal retinal function depends on a continuous supply of oxygen and on the capability to detect and respond rapidly to local oxygen deficiency or hypoxia. Retinal hypoxia can cause retinal dysfunction and degeneration that lead directly to vision loss. In this section, the role of retinal oximetry in retinal pathologies and the overall technological progress in measuring retinal oximetry is presented.

2.3.1 Retinal diseases and oxygenation

Most major retinal pathologies mentioned in section 1.1.2 cause alteration in the retinal oxygenation. For example, both retinal vessel occlusions (RVO) and diabetic retinopathy (DR) cause hypoxia [39]. Several changes are induced in the retina during hypoxia, most prominent being the vascular endothelial growth factor or VEGF. There are reports about the increase in VEGF in DR by various investigators [40, 41]. Another change which happens as a result of hypoxia in the retina is over-expression of Hypoxia inducible factor 1 or HIF1 [42, 43].

Retinal vessel occlusions result in a decrease in blood flow in the retina and thus affects oxygenation starting from capillary level [44] and can be seen with a fundus camera when the occlusion reaches artery or vein level. However, it is difficult to reliably and accurately measure oxygen saturation in small vessels with a fundus camera. SLOs are expected to perform better for diagnosis and follow-ups on vessel occlusions in small capillaries due to increased resolution. Retinal oxygen saturation is considered as an independent risk factor for the severity of diabetic retinopathy [45]. DR causes damage to the retinal capillaries and microaneurysms, causing reduced blood flow and hypoxia. The major result of hypoxia

in the retina is neovascularisation. The retina tries to grow new vessels in response to hypoxia. The new vessels pose a risk of haemorrhage due to their fragility.

Glaucoma is another disease where oxygen metabolism is affected. Glaucoma causes an increase in intraocular pressure (IOP), which in turn affects the blood flow [46]. Vandewalle *et al.* [47] reported that the arterio-venule (A-V) difference in oxygen saturation decreased as the rim area and the nerve fiber layer decreased in glaucomatous patients. Since Glaucoma treatment alters the blood flow and IOP, oximetry measurements before and after glaucoma treatment may help to understand the role of blood flow and oxygen saturation in glaucoma [48]. For example, it is very valuable to investigate whether a glaucoma patient receives enough blood flow and oxygenation after treatment. Age-related macular degeneration (AMD) is the leading cause of irreversible blindness throughout the world. Ageing and age-associated degenerative diseases, such as AMD, are intimately associated with decreased levels of tissue oxygenation and hypoxia that may induce accumulation of detrimental RPE-associated deposits, inflammation and neovascularisation processes in the retina.

2.3.2 Evolution of retinal oximetry

There has been a need for better instruments for oxygen measurements in the retina over the past few decades. The earliest attempts at *in vivo* retinal oximetry started in the 1960's based on work by Hickam *et al.* [49, 50]. Significant developments in the field came when François Delori developed a 3 wavelength retinal oximetry method that could operate continuously [51]. Delori determined oxygen saturation by scanning a focused point of light across the vessel, allowing both the vessel diameter and the optical density of the blood to be calculated from the profile of the reflected light. Vessel tracking was used to minimise the effects of eye movements during scanning.

Smith *et al.* [52] developed a prototype eye oximeter (Fig. ??(a)) to study the effect of blood loss on retinal venous oxygen saturation, with a goal to apply their technique to monitoring trauma patients [52]. Two diode lasers emitting at 670 nm and 803 nm were initially used in the eye oximeter (EOX) to produce a line scan of a retinal vessel. A photodiode was used to measure the reflected light from the retina and blood vessel. An imaging ophthalmic-spectrometer was developed by Schweitzer *et al.* to analyse the spectral reflection of pigments such as melanin, and xanthophyll in the fundus. The reflectance spectrum in the range from 450 nm to 700 nm with a spectral resolution of 2 nm was acquired from a small area using a spectrograph. The measurement of the oxygen saturation in retinal vessels in-

volved extensive analysis of the properties of fundus reflectance and the multiple light pathways in the retina [53]. The mean oxygen saturation was found to be 92.2 ± 4.1 % for arterial blood and 57.9 ± 9.9 % for venous blood. Beach *et al.* [54] attempted two-wavelength oximetry using an isosbestic wavelength and oxygen-sensitive wavelength in a fundus camera. They also attempted to calibrate the oxygen saturation values based on vessel diameters and pigmentation in the fundus.

In the past decade two commercially available retinal oximetry systems— the Oxymap retinal oximeter (Oxymap ehf, Iceland) [55] and the Imedos retinal oximeter (Imedos Systems UG, Germany) [56] (Fig. 2.9) have been used for various clinical studies to measure oxygenation under different retinal pathologies.

A critical factor for clinically relevant retinal oximetry is to be able to determine blood oxygen saturation in small retinal vessels — capillaries, venules and arterioles. It is in these microvessels that the oxygen saturation is expected to decrease in response to increased metabolic demand or decreased oxygen delivery capacity. The larger retinal vessels ($>100 \mu\text{m}$) are expected to be less sensitive to changes in tissue metabolic demand or microvascular dysfunction and are therefore not ideal as early hypoxia markers.

Spectral Domain optical coherence tomography (SD-OCT) based on visible wavelengths [22, 23, 59] has been used to measure oxygenation in retinal blood vessels. Recent intense and broadband supercontinuum light sources have made it possible to perform OCT in the visible wavelength regime. Visible light OCT enables oxygen saturation mapping and has a higher axial resolution for a given wavelength bandwidth compared to 800 nm or 1000 nm OCT. Higher absorption and scattering of the retina at visible wavelengths limit penetration depths. Further, Supercontinuum light source used in visible OCT systems introduces significant amounts of relative intensity noise.

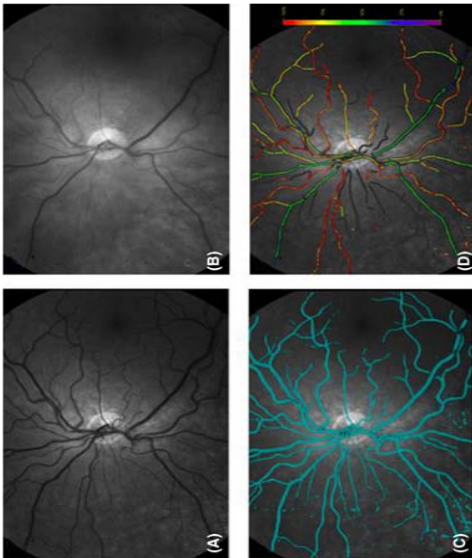
Various groups have also undertaken hyperspectral imaging [60–63] approaches towards in vivo retinal oximetry. However, acquiring images with sufficient SNR from multiple wavelengths at high spatial resolution remains a challenge in hyperspectral imaging.

2.3.3 Comparison of oximetry techniques

SLO based oximetry systems have advantages over other techniques based on fundus camera based multispectral or hyperspectral imaging. As mentioned in section 2.2, SLOs are capable of producing high contrast, confocal images due to scanning and use of a confocal pinhole. SLOs also typically use lasers to create monochromatic images at multiple wavelengths, and minimise unnecessary exposure of light

Dual wavelength fundus cameras

(a) Oxymap ehf. (Iceland)



(b) Imedos systems GmbH (Germany)

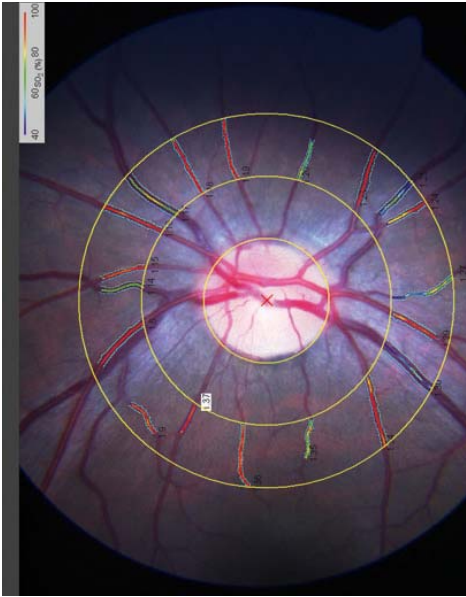


Figure 2.9: (a): the Oxymap retinal oximeter (Reykjavik, Iceland) using 570 nm and 600 nm wavelengths to map the oxygen saturation values (b):Retinal oxygen saturation measurement by Imedos UG, Jena, Germany. (images taken from Rilven *et. al.* [57] and Man *et al.* [58])

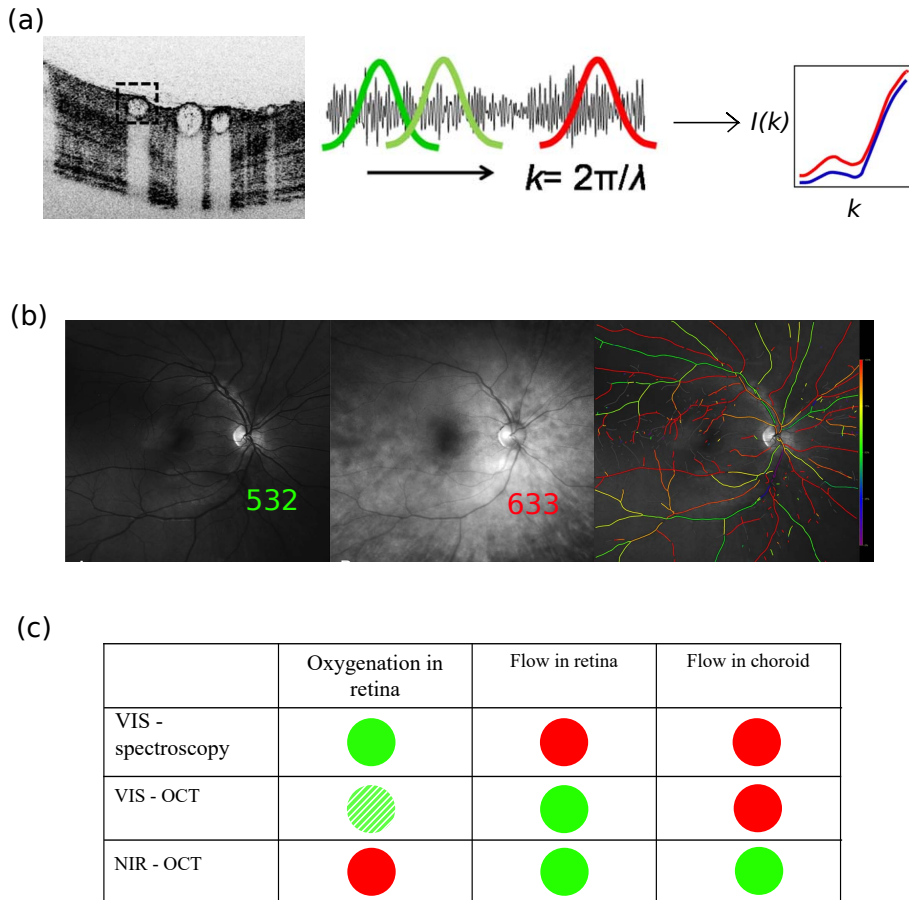


Figure 2.10: (a): Illustration of visible light OCT retinal oximetry showing a OCT b-scan. A Fourier transform is used to convert the intensity in the bottom of the blood vessel into spectral information, which is then fit per wave number (k) to extract the oxygen saturation measurement— illustration was adapted from Yi *et al.*[59]. (b):Retinal oxygen saturation measurement by Optomap 200Tx using 532 nm and 633 nm wavelengths. The images are then analysed using oximetry algorithm to extract oxygen saturation values (images from Kristjansdottir *et al.* [64]). (c) Table showing the potential of spectroscopic and OCT based techniques for retinal oxygenation and flow measurements; green and red circles represent technological possibility and impossibility respectively.

to the fundus, unlike the fundus camera-based oximeters where broadband light is typically used and spectral filtering is performed in the detection. With suitable optics, wide-field scanning of almost the entire fundus is possible with an SLO (Fig. 2.10(b)), whereas conventional fundus cameras are limited to relatively narrow images of the posterior pole [64]. A major drawback of SLO based oximetry is the lack of available lasers at optimum wavelengths which have been addressed in chapter 5 of this thesis.

Visible light OCT offers the prospect of functional retinal imaging, as most retinal chromophores possess distinct absorption signatures at visible wavelengths. An illustration of visible light OCT retinal oximetry is shown in Fig. 2.10(a). Quantifying oxygen saturation using visible OCT is considered more advantageous than using Near infrared (NIR) OCT due to the high absorption of blood in the visible range compared to 800 nm or 1050 nm. Visible OCT can measure the flow in the retina [22], but the penetration of visible light into the retina is limited, and visible OCT is incapable of measuring choroidal flow.

Further, OCT being a coherent detection scheme suffers from speckles, and a significant amount of averaging has to be performed to reduce the speckle contrast. The spectral bands (Fig. 2.10) extracted from the OCT signal of the blood vessels should be wide enough to ensure good signal-to-noise ratio of individual spectral bands to get a good fit of the absorption spectrum. However, the absorption of Hb in the visible range is a fast-changing function of wavelength (Fig. 2.5(b)), and smaller bands are thus required to get an accurate fit. All current OCT systems are based on supercontinuum sources which suffer from excess noise or RIN noise [22]. These factors make SLOs attractive for retinal oximetry. Another significant advantage is that SLOs with two or more wavelengths can be easily integrated with the NIR OCT modules operating at 1050 nm to get the overall oxygen metabolism of the retina and the blood flow in the choroid. Substantially higher amounts of light can be used for OCT imaging at longer wavelengths (as explained in section 2.2.2) compared to visible wavelengths, which make the combination of visible SLO and NIR OCT more viable.

References

- [1] R. H. Webb, G. W. Hughes, and F. C. Delori, "Confocal scanning laser ophthalmoscope.," *Appl. Opt.* **26**, 14921499 (1987).
- [2] M. Rajadhyaksha, R. R. Anderson, and R. H. Webb, "Video-rate confocal scanning laser microscope for imaging human tissues in vivo.," *Appl. Opt.* **38**, 21052115 (1999).
- [3] D. X. Hammer, R. D. Ferguson, T. E. Ustun, C. E. Bigelow, N. V. Iftimia, and R. H. Webb, "Line-scanning laser ophthalmoscope.," *J. Biomed. Opt.* **11**, 041126 (2014).
- [4] A. E. Elsner, S. A. Burns, G. W. Hughes, and R. H. Webb, "Reflectometry with a scanning laser ophthalmoscope," *Appl. Opt.* **31**, 36973710 (1992).
- [5] M. Damodaran, K. V. Vienola, B. Braaf, K. A. Vermeer, and J. F. de Boer, "Digital micromirror device based ophthalmoscope with concentric circle scanning," *Biomed. Opt. Express* **8**, (2017).
- [6] K. Vienola, M. Damodaran, B. Braaf, K. Vermeer, and J. F. J. de Boer, "Parallel line scanning ophthalmoscope for retinal imaging," *Opt. Lett.* **40**, 53355338 (2015).
- [7] S. Stephen, *Optical systems for laser scanners*, in *Handbook of Optical and Laser Scanning*, 2nd ed., pp. 69132, CRC Press, Boca Raton, FL (2011).
- [8] Spatial light modulator and method, US patent no. 4566935 (1986).
- [9] M. S. Muller, J. J. Green, K. Baskaran, A. W. Ingling, J. L. Clendenon, T. J. Gast, and A. E. Elsner, "Non-mydriatic confocal retinal imaging using a digital light projector," *Proc. SPIE.* **9376**, 93760E (2015).
- [10] B. Lochocki, A. Gambin, S. Manzanera, E. Irls, E. Tajahuerce, J. Lancis, and P. Artal, "Single pixel camera ophthalmoscope," *Optica* **3**(10), 1056-1059 (2016).
- [11] M. A. Davis, "Hardware triggering: maximising speed and efficiency for live cell imaging," *Nat. Methods* **14**, iii (2017).
- [12] T. Garcia, DLP5531-Q1 Chipset Video Processing for Light Control Applications (2018).
- [13] J. Tabernero, A. Benito, E. Alcón, and P. Artal, "Mechanism of compensation of aberrations in the human eye.," *J. Opt. Soc. Am. A. Opt. Image Sci. Vis.* **24**, 3274-83 (2007).
- [14] E. J. Fernández, A. Unterhuber, B. Povaay, B. Hermann, P. Artal, and W. Drexler, "Chromatic aberration correction of the human eye for retinal imaging in the near infrared," *Opt. Express* **14**, 6213 (2006).
- [15] L. N. Thibos, A. Bradley, and X. Zhang, The effect of ocular chromatic aberration on monocular visual performance, *Optom. Vision Sci.* **68**, 599-607 (1991).
- [16] D. A. Atchinson and G. Smith, Chromatic dispersions of the ocular media of human eyes, *J. Opt. Soc. Am. A* **22**, 29-36 (2005).
- [17] P. A. Howarth, X. X. Zhang, A. Bradley, D. L. Still, and L. N. Thibos, Does the chromatic aberration of the eye vary with age?, *J. Opt. Soc. Am. A* **5**, 2087-2092 (1988).
- [18] C. Ware, Human axial chromatic aberration found not to decline with age, *A. Graefes Arch. Klin. Exper. Ophthalmol.* **218**, 39-41 (1982).

- [19] I. Powell, "Lenses for correcting chromatic aberration of the eye," *Appl. Opt.* **20**, 2-5 (1981).
- [20] R. J. Zawadzki, B. Cense, Y. Zhang, S. S. Choi, D. T. Müller, and J. S. Werner, "Ultrahigh-resolution optical coherence tomography with monochromatic and chromatic aberration correction," *Opt. Express* **16**, 1734-1746 (2008).
- [21] F. LaRocca, D. Nankivil, S. Farsiu, and J. A. Izatt, "True color scanning laser ophthalmoscopy and optical coherence tomography handheld probe," *Biomed. Opt. Express* **5**, 3204 (2014).
- [22] S. P. Chong, M. Bernucci, H. Radhakrishnan, and V. J. Srinivasan, "Structural and functional human retinal imaging with a fiber-based visible light OCT ophthalmoscope," *Biomed. Opt. Express* **8**, 323 (2017).
- [23] S. P. Chong, T. Zhang, A. Kho, M. T. Bernucci, A. Dubra, and V. J. Srinivasan, "Ultrahigh resolution retinal imaging by visible light OCT with longitudinal achromatization," *Biomed. Opt. Express* **9**, 1477 (2018).
- [24] J. A. Díaz, C. Pizarro, and J. Arasa, "Single dispersive gradient-index profile for the aging human lens," *J. Opt. Soc. Am. A* **25**, 25061 (2008).
- [25] F. C. Delori, and K. P. Pflibsen, "Spectral reflectance of the human ocular fundus" *Appl. Opt.* **28**, 1061-77 (1989).
- [26] M. Hammer, A. Roggan, D. Schweitzer, G. Müller, and G. Müller, "Optical properties of ocular fundus tissues—an in vitro study using the double-integrating-sphere technique and inverse Monte Carlo simulation," *Phys. Med. Biol.* **40**, 963-78 (1995).
- [27] A. N. Schechter, Hemoglobin research and the origins of molecular medicine, *blood*, **112**(10), 3927-3938 (2008).
- [28] M. Friebe and M. Meinke, Determination of the complex refractive index of highly concentrated hemoglobin solutions using transmittance and reflectance measurements, *J. Biomed. Opt.* **10**, 640-19 (2005).
- [29] A. Amelink, T. Christiaan, and H. J. C. M. Sterenborg, "Effect of hemoglobin extinction spectra on optical spectroscopic measurements of blood oxygen saturation," *Opt. Lett.* **34**, 15251527 (2009).
- [30] N. Bosschaart, G. J. Edelman, M. C. G. Aalders, T. G. van Leeuwen, and D. J. Faber, "A literature review and novel theoretical approach on the optical properties of whole blood," *Lasers Med. Sci.* **29**, 453479 (2014).
- [31] F. C. Delori, R. H. Webb, and D. H. Sliney, "Maximum permissible exposures for ocular safety (ANSI 2000), with emphasis on ophthalmic devices," *J. Opt. Soc. Am. A* **24**, 1250 (2007).
- [32] D. H. Sliney, Retinal injury from laser radiation, *Nonlinear Opt.* **21**, 117 (1999).
- [33] D. J. Lund, Action spectrum for retinal thermal damage, in *Measurements of Optical Radiation Hazards*, R. Matthes and D. Sliney, eds. (International Commission on NonIonizing Optical Radiation, 1998), pp. 209228.
- [34] W. T. J. Ham and H. A. Mueller, The photopathology and nature of the blue light and near-UV retinal lesions produced by lasers and other optical sources, in *Laser Applications in Medicine and Biology*, M. L. Wolbarsht, ed. (Plenum, 1989), pp. 191246.
- [35] B. E. Stuck, The retina and action spectrum for photoretinitis, in *Measurements of Optical Radiation Hazards*, R. Matthes and D. Sliney, eds. (International Commission on Non-Ionizing Optical Radiation, 1998), pp. 193208.
- [36] International Electrotechnical Commission, Safety of Laser Products Part 1: Equipment Classification and Requirements, (Geneva, Switzerland), IEC-60825-1 (2014).
- [37] European Machine Vision Association, "EMVA Standard 1288 - 3.0: Standard for characterisation of Image Sensors and Cameras," **82** (2012).
- [38] J. H. Parsons, The Ocular Circulation Bale and Danielsson (1903).
- [39] O. Arjamaa and M. Nikinmaa, "Oxygen-dependent diseases in the retina: role of hypoxia-inducible

- factors," *Exp Eye Res*, **83**(3), 473-483.(2006).
- [40] H. Noma, H. Funatsu, T. Mimura, M. Tatsugawa, K. Shimada, and S. Eguchi, "Vitreous Inflammatory Factors and Serous Macular Detachment in Branch Retinal Vein Occlusion," *Retina*, **32**(1), 86-91. (2012).
- [41] L. P. Aiello, R. L. Avery, P. G. Arrigg, B. A. Keyt, H. D. Jampel, S. T. Shah, L. R. Pasquale, H. Thieme, M. A. Iwamoto, J. E. Park, "Vascular endothelial growth factor in ocular fluid of patients with diabetic retinopathy and other retinal disorders," *N Engl. J. Med.*, **331**(22), 1480-1487 (1994).
- [42] C. A. K. Lange and J. W. B. Bainbridge, "Oxygen sensing in retinal health and disease," *Ophthalmologica* **227**00, 115131 (2012).
- [43] O. Arjamaa, M. Nikinmaa, A. Salminen, and K. Kaarniranta, "Regulatory role of HIF-1 α in the pathogenesis of age-related macular degeneration (AMD)," *Ageing Res. Rev.* **8**, 349358 (2009).
- [44] S. Yoneya, T. Saito, Y. Nishiyama, T. Deguchi, M. Takasu, T. Gil, and E. Horn, "Retinal oxygen saturation levels in patients with central retinal vein occlusion," *Ophthalmology*, **109**(8), 1521-1526 (2002).
- [45] T. Bek, E. Stefansson, and S. H. Hardarson, "Retinal oxygen saturation is an independent contributor to the severity of retinopathy in diabetic patients," *Br. J. Ophthalmol.* (2018).
- [46] D. Schmidl, G. Garhofer, and L. Schmetterer, "The complex interaction between ocular perfusion pressure and ocular blood flow - Relevance for glaucoma". *Exp Eye Res*, **93**(2), 141-155. (2011).
- [47] E. Vandewalle, L. A. Pinto, O. B. Olafsdottir, E. De Clerck, P. Stalmans, J. Van Calster, T. Zeyen, E. Stefansson, and I. Stalmans, "Oximetry in glaucoma: Correlation of metabolic change with structural and functional damage," *Acta Ophthalmol.* **92**, 105-110 (2014).
- [48] S. Traustason, S. H. Hardarson, M. S. Gottfredsdottir, T. Eysteinnsson, R. A. Karlsson, E. Stefansson, and A. Harris, "Dorzolamide-timolol combination and retinal vessel oxygen saturation in patients with glaucoma or ocular hypertension," *Br. J. Ophthalmol.* **93**, 10641067 (2009).
- [49] J. B. Hickam, H. O. Sieker, and R. Frayser, "Studies of retinal circulation and A-V oxygen difference in man.," *Trans. Am. Clin. Climatol. Assoc.* **71**, 3444 (1959).
- [50] J. B. Hickam, R. Frayser, and J. C. Ross, "A study of retinal venous blood oxygen saturation in human subjects by photographic means," *Circulation* **27** 37585 (1963).
- [51] F. C. Delori, "Noninvasive technique for oximetry of blood in retinal vessels.," *Appl. Opt.* **27**, 1113-1125 (1988).
- [52] M. H. Smith, K. R. Denninghoff, L. W. Hillman, and R. A. Chipman, "Oxygen saturation measurements of blood in retinal vessels during blood loss," *J. Biomed. Opt.* **3**, 296-303 (1998).
- [53] D. Schweitzer, M. Hammer, J. Kraft, E. Thamm, E. Königsdörffer, and J. Strobel, "In vivo measurement of the oxygen saturation of retinal vessels in healthy volunteers.," *IEEE Trans. Biomed. Eng.* **46**, 1454-1465 (1999).
- [54] J. M. Beach, K. J. Schwenzer, S. Srinivas, D. Kim, and J. S. Tiedeman, "Oximetry of retinal vessels by dual-wavelength imaging: calibration and influence of pigmentation," *J. Appl. Physiol.* **86** 748-58 (1999).
- [55] S. H. Hardarson, A. Harris, R. A. Karlsson, G. H. Halldorsson, L. Kagemann, E. Rechtman, G. M. Zoega, T. Eysteinnsson, J. A. Benediktsson, A. Thorsteinsson, P. K. Jensen, J. Beach, and E. Stefansson, "Automatic retinal oximetry," *Investig. Ophthalmol. Vis. Sci.* **47**, 5011-5016 (2006).
- [56] M. Hammer, W. Vilser, T. Riemer, A. Mandecka, D. Schweitzer, U. Kühn, J. Dawczynski, F. Liemt, and J. Strobel, "Diabetic patients with retinopathy show increased retinal venous oxygen saturation," *Graefes Arch. Clin. Exp. Ophthalmol.* **247** 1025-1030 (2009).
- [57] S. Rilven, T. L. Torp, and J. Grauslund, "Retinal oximetry in patients with ischaemic retinal diseases," *Acta Ophthalmol.* **95**, 119-127 (2017).
- [58] R. E. Man, R. Kawasaki, Z. Wu, C. D. Luu, J. J. Wang, T. Y. Wong, and E. L. Lamoureux, "Reliability

- and reproducibility of retinal oxygen saturation measurements using a predefined peri-papillary annulus," *Acta Ophthalmol* **91**, 590-594 (2013).
- [59] J. Yi, Q. Wei, W. Liu, V. Backman, and H. F. Zhang, "Visible-light optical coherence tomography for retinal oximetry," *Opt. Lett.* **38**, 1796-1798 (2013).
- [60] J. C. Ramella-Roman, S. a Mathews, H. Kandimalla, A. Nabili, D. D. Duncan, S. a DAnna, S. M. Shah, and Q. D. Nguyen, "Measurement of oxygen saturation in the retina with a spectroscopic sensitive multi aperture camera.," *Opt. Express* **16**, 6170-6182 (2008).
- [61] W. R. Johnson, D. W. Wilson, W. Fink, M. Humayun, and G. Bearman, "Snapshot hyperspectral imaging in ophthalmology.," *J. Biomed. Opt.* **12**, 01403-6 (2014).
- [62] B. Khoobehi, J. M. Beach, and H. Kawano, "Hyperspectral Imaging for Measurement of Oxygen Saturation in the Optic Nerve Head," *Invest. Ophthalmol. Vis. Sci.* **45**, 1464-72 (2004).
- [63] J. Beach, J. Ning, and B. Khoobehi, "Oxygen saturation in optic nerve head structures by hyperspectral image analysis.," *Curr. Eye Res.* **32**, 161-170 (2007).
- [64] J. V. Kristjansdottir, S. H. Hardarson, G. H. Halldorsson, R. A. Karlsson, T. S. Eliasdottir, and E. Stefánsson, "Retinal oximetry with a scanning laser ophthalmoscope," *Investig. Ophthalmol. Vis. Sci.* **55**, 3120-3126 (2014).